25-27 September 2012, Budapest, Hungary

Nanoscale Electrothermal Energy Conversion Devices

Je-Hyeong Bahk[1,2], Younes Ezzahri[2,3], Kazuaki Yazawa[1,2], Bjorn Vermeersch[1,2], Gilles Pernot[2,4], Ali Shakouri[1,2,*]

[1] Birck Nanotechnology Center, Purdue University, 1205 West State Street, West Lafayette, IN 47907-2057, USA
[2] Baskin School of Engineering, University of California Santa Cruz, CA 95064-1077, USA
[3] Département Fluides, Thermique, Combustion, Institut Pprime, CNRS-Université de Poitiers-ENSMA, ENSIP Bâtiment de mécanique, 2 rue Pierre Brousse, F86022 Poitiers Cedex, France.
[4] LOMA, Université de Bordeaux, 33400 Talence, France
[*] Shakouri@purdue.edu

***Abstract*- Energy consumption in our society is increasing rapidly. A significant fraction of the energy is lost in the form of heat. In this talk we introduce thermoelectric devices that allow direct conversion of heat into electricity. Some new physical concepts and nanostructures make it possible to modify the trade-offs between the bulk electrothermal material properties through the changes in the density of states, scattering rates, and interface effects on the electron and phonon transport. The potential to increase the energy conversion efficiency and bring the cost down to $0.1-0.2/W will be discussed. We also describe how similar principles can be used to make micro refrigerators with cooling power densities exceeding 500 Watts per square centimeter. Hybrid liquid/solid-state cooling will be shown to have the potential to reduce the total cooling power requirement significantly by selective removal of hot spots. Finally, experimental results will be presented for thin film thermal conductivity of nanostructured materials using a femtosecond laser pump-probe technique. We describe how the ballistic and diffusive components of heat transport can be identified. The transition between energy and entropy transport in nanoscale devices will be discussed.**

I. INTRODUCTION

Thermoelectric is a solid-state energy conversion technique that can directly convert heat to electricity and vice versa. Since the working fluid is electrons/holes, thermoelectric devices have many unique advantages over conventional energy conversion systems including: no moving parts or vibration, high reliability and durability, compactness, and easy control.[1] It is thus very useful for various applications such as hot-spot cooling on micro-chips, and electrical power generation from waste heat. The energy conversion efficiency of thermoelectric devices is directly related to the thermoelectric figure of merit, $ZT=S^2\sigma T/(\kappa_e+\kappa_l)$, of the materials used, where S is the Seebeck coefficient, σ is the electrical conductivity, T is the absolute temperature, and κ_e and κ_l are the electronic and lattice thermal conductivities, respectively. If ZT is larger than 3-5, the thermoelectric device can be competitive with traditional mechanical energy conversion systems. In the 1950s, Bi_2Te_3 alloys were found to have ZT~1 at room temperature, but since then, the progress has been slow because all the properties comprising ZT are mutually coupled, and it is extremely difficult to enhance one property without affecting another.

Recent advances in the material synthesis and growth techniques and pioneering theoretical studies have enabled breakthroughs for the enhancement of thermoelectric materials beyond ZT~1. In the early 1990s, Hicks and Dresselhaus [2] theoretically predicted a significant enhancement of ZT in low-dimensional materials such as quantum wells and wires. Since their work, along with timely availability of advanced materials, a great deal of research on nanostructured materials has been conducted for thermoelectric applications.[3,4] Indeed significant improvements of ZT values have been reported during the past few decades. However, most of the improved ZT values were achieved mainly by the reduction of lattice thermal conductivity, and the significant enhancement of thermoelectric power factor, $S^2\sigma$, has not been realized to date. We will discuss several difficulties as well as future directions for the power factor enhancement and, in Section II, summarize the recent results of ZT enhancement achieved for various nanostructured materials.

Applications of TE devices have been limited due to their low energy conversion efficiency. An important factor for any energy conversion device is cost per watt analysis. Yazawa and Shakouri [5] recently analyzed the cost-efficiency trade-off of TE devices and found that TE devices can be competitive with other sustainable energy technologies in terms of cost per watt even with the current efficiency values when the design of the device is optimized. We revisit the cost analysis of TE devices in Section III.

Another advantage of TE devices is their ability to be combined with other conventional liquid cooling techniques [6], which offer an additional degree of freedom for removing both background heating and hot spots in integrated circuit chips. Hot spots and non-uniform temperature distribution in the chip can degrade the performance and reduce the reliability. Unfortunately, most of the existing cooling techniques cannot remove the hot spots selectively and they have to operate in a suboptimal fashion and overcool the entire chip [7]. To overcome these difficulties, one solution is to use hybrid solid-state and liquid cooling, which is described in Section IV.

Time domain thermoreflectance (TDTR) is a femtosecond pulsed laser technique capable of characterizing thermal properties of thin films [8,9] and therefore highly valuable to

 ISBN:978-2-35500-022-5

assess the performance of thermoelectric materials [10-12]. Thermoreflectance imaging is another thermal characterization technique utilizing optical measurement of the variation of light reflectivity with temperature on the illuminated surface. Using a high resolution CCD camera, temperature mapping is possible without a scan. Joule heating and Peltier cooling can be separated since they have different dependencies on the magnitude and direction of current. Thermal conductivity measurements of thin film nanostructured materials using TDTR and the details of the two characterization techniques will be discussed in Sections V and VI.

Based on Shastry's work [13], we analyze both the ballistic (non-thermal) and diffusive (thermal) energy transport by electrons in metals occurring for a very short period of time. It is found that a damped oscillatory behavior of the energy density, Green's function, due to the ballistic transport is dominant at very short time less than the scattering time and at very short length scale, and then disappears as the diffusive transport becomes significant. Both spatial and temporal impulse responses are obtained and analyzed to separate the ballistic and diffusive components of the transport in Section VII. Finally, a summary is followed to conclude the paper.

II. Nanostructured Thermoelectric Materials

The theoretical prediction of a large ZT enhancement in quantum wells and wires by Hicks and Dresselhaus [2] is based on the enhancement of the thermoelectric power factor due to the modification of the electronic density of states in the in-plane direction of those low-dimensional materials. The quantum confinement in the low-dimensional materials creates sharp features in the density of states, which increases the asymmetry in the differential conductivity with respect to the Fermi energy, thereby enhancing the Seebeck coefficient.[14] However, most of the recently reported ZT enhancements did not come from the power factor enhancement. Lattice thermal conductivity was reduced due to the increased interface and boundary scattering of phonons in the nanostructured materials. Some of the reasons that an enhancement of the in-plane power factor in quantum wells or along nanowires is practically difficult could be: 1) increased carrier scattering at the interfaces, which reduces the electrical conductivity, 2) quick disappearing of the sharp features in the density of states due to size non-uniformity in the confinement directions, 3) the reduction of band degeneracy due to the quantum confinement, and 4) the wide distribution of carrier energy compared to the width of the sharp features in the density of states. Furthermore, Kim et al.[15] recently pointed out in their theoretical calculations based on the Landauer formalism that the enhancement in Seebeck coefficient is modest and the major improvement, at most 50% over bulk, comes from the enhancement in effective 3D electrical conductivity in a lower dimensional system with a high packing density.

In the cross-plane direction of superlattices, two scenarios for the Seebeck coefficient enhancement may be possible. Firstly, low-energy carriers can be filtered out of the transport due to the presence of potential barriers in the cross-plane direction of heterostructure superlattices. Hot electrons having energies higher than the barrier height can go over the barriers and contribute to the transport. This energy filtering scheme can enhance the Seebeck coefficient [16, 17] Theoretical calculations showed that a large enhancement of Seebeck coefficient and, thus, ZT is possible when the lateral momentum of carriers is not conserved during the transport over barriers.[18] If the lateral momentum is conserved in analogy with the total internal reflection of light, the emission current over the barrier could be so low that the power factor may not be largely enhanced even with the large Seebeck enhancement. Also, the number of conducting channels in both the well and barrier layers can be a limiting factor in enhancing the power factor.[19] Secondly, when the superlattice period is much smaller than the mean free path of carriers, coherent multiple interferences by the periodic superlattice potential can form mini-bands, which modify the density of states, and thus, can enhance the Seebeck coefficient.[20, 21] A large enhancement of Seebeck coefficient was predicted at low temperatures in the miniband transport regime, but the power factor was not enhanced due to the suppression of group velocity of carriers.[21] However, further optimization of design and selection of materials may be possible to lead to power factor enhancement, even at room temperature or higher.

In the materials with embedded nanoparticles, modification of carrier scattering time by nanoparticle scattering can enhance the power factor.[22-24] Ionized nanoparticles create spatially slowly-varying potentials around them, which are different from the potential by conventional ionized impurities. The actual enhancement of power factor comes from the increased electrical conductivity at a given Seebeck coefficient, rather than the Seebeck enhancement.[24] Core-shell nanoparticles can create energetically sharp scattering characteristics via resonances, which can significantly enhance the Seebeck coefficient at low temperatures.[25] Recently a modulation doping concept was proposed to enhance the electrical conductivity and thus, the power factor.[26] Heremans et al. demonstrated a large power factor enhancement in Tl-doped PbTe at high temperatures up to 770 K, and attributed this enhancement to the distorted density of states by the Tl resonant level inside the valence band of PbTe.[27] The ErAs:InGaAlAs semimetal/semiconductor nanocomposites showed enhanced ZT~1.3 at 800 K over bulk InGaAlAs due mainly to the thermal conductivity reduction by increased phonon scattering by a few nm-sized ErAs nanoparticles.[28]

Fig. 1 shows several important ZT values, both n- and p-type, that were recently reported for nanostructured materials over a wide temperature range. The ZT values of the conventional thermoelectric materials such as Bi_2Te_3, PbTe, and SiGe are also shown in the figure for comparison. ZTs of about 1.5-1.7 have been reported in several different nanostructured materials in the last ten years. ZTs higher than 2 were also reported in a few cases, but further experimental verification is necessary as some of the data are not independently verified [3]. It is noted that most of the ZT improvements in Fig. 1 were obtained via reduction of the lattice thermal conductivity, except for the two cases [26,27]

in which enhanced power factor was the main factor leading to high ZTs.

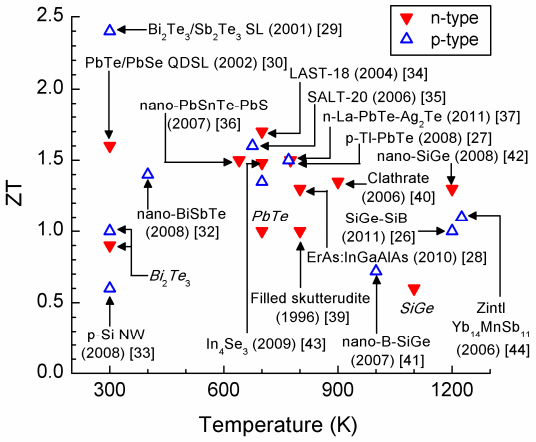

Fig. 1. Advances of thermoelectric figure of merit, ZT, reported over a temperature range from 300 K to 1200 K.

At near room temperature or 300 K, Bi_2Te_3 or PbTe-based nanostructured materials showed significant enhancement in ZT over their bulk counterparts by a reduction of thermal conductivity. The Bi_2Te_3/Sb_2Te_3 superlattice [29] was reported to have a cross-plane thermal conductivity value of 0.22 W/mK, which is more than two times lower than that of $Bi_{0.5}Sb_{1.5}Te_3$ alloy, and attributed to the increased interface phonon scattering in the superlattice. A large ZT of 2.4 was reported for this superlattice, but to our best knowledge, this value has not been reproduced. PbTe/PbSe nano-dot superlattices by Harman et al. [30] showed ZT~1.6 at this temperature due to the very low thermal conductivity of 0.33 W/mK that was inferred indirectly from thermoelectric cooling measurements. Recent direct measurements using the time-domain thermoreflectance technique, however, did not reproduce this value.[31] Recently, nanostructured p-type BiSbTe bulk alloys prepared by hot pressing ball-milled nanopowders showed ZT~1.2 at room temperature and ~1.4 near 400 K.[32] Recently, Hochbaum et al. fabricated and measured rough silicon nanowires of ~50 nm in diameter, which showed a ZT ~ 0.6 at room temperature.[33] This ZT value is still lower than 1, but is significantly higher than the ZT ~ 0.01 of bulk silicon.

At elevated temperatures, near 600 K or higher, several PbTe-based nanostructured materials showed high ZTs of 1.5~1.7 over the best bulk PbTe of ZT~1. The material system, $AgPb_mSbTe_{2+m}$, also known as LAST-m, becomes spontaneously nanostructured when cooled from the melt, which helps reduce the thermal conductivity. With selected m values, e.g. LAST-18, the thermal conductivity was found to be only about 30% of that of PbTe, and thus a ZT~1.7 at 700 K was achieved.[34] A p-type variation of LAST-m, $NaPb_mSbTe_{2+m}$ (SALT-m), also showed ZT~1.6 at 675 K for m~20 with a very low thermal conductivity of 0.85 W/mK.[35] The strain field created by nano-inclusions in these material system is believed to scatter phonons effectively to reduce the thermal conductivity. The $(PbSnTe)_x(PbS)_{1-x}$ system is phase-separated into PbTe-rich and PbS-rich regions, which become coherent nanostructures suppressing the lattice thermal conductivity. A ZT ~ 1.5 at 640 K was reported for this material system of n-type with x~0.08.[36] The n-type La-doped Ag_2Te-PbTe system has nano-scale (50-200 nm) Ag2Te precipitates formed in PbTe, and showed ZT~1.5 at 775 K.[37] Skutterudites and clathrates have complex cage-like crystal structures with voids in which 'rattler' atoms are inserted to effectively scatter acoustic phonons.[38] $CoSb_3$-based filled skutterudites such as p-type $LaFe_3CoSb_{12}$, and n-type $CeFeCoSb_{12}$ showed ZT > 1 at 800 K and higher.[39] Recently, Czochralski-grown clathrate $Ba_8Ga_{16}Ge_{30}$ showed ZT~1.6 at 1100 K. [40]

Beyond 1000 K, SiGe has long been known to be a good thermoelectric material, and its ZT is typically 0.5 ~ 0.6 at 1100 K. After nanostructuring by hot pressing and ball milling, ZT of p-type B-doped SiGe was improved to 0.7 at 1000 K.[41] ZT~1.3 at 1200 K was also reported for nanostructured n-type SiGe. [42] Two-phase SiGe-SiP nanocomposites had ZT > 1 at 1200 K, and this ZT enhancement was attributed to the modulation doping effect that enhanced mobility and thus electrical conductivity.[26]

III. Cost Analysis of Thermoelectric Devices

Energy conversion from a waste heat is important since we are dissipating more than half of the energy from natural resources. Thermoelectric is suitable for this application due to relatively lower operating temperature compared to mechanical systems. Fig. 2 shows the one-dimensional model that we used for theoretical analysis [5].

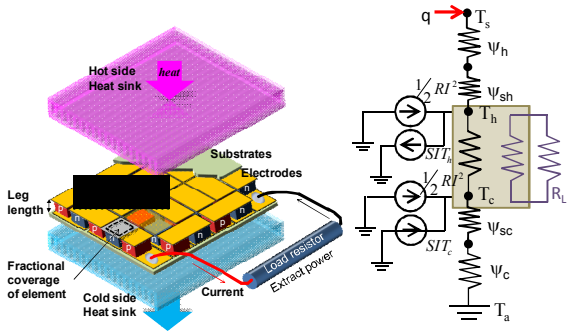

Fig. 2. Thermoelectric waste heat power generation system and electro-thermal network model.

Since the heat source is free of cost, the minimum mass of the material used to produce the maximum power output is the criteria to finding the lowest cost per useful energy produced. The maximum power output, W_{max}, is found in Eq. (1) to be proportional to the square of overall temperature difference from the heat source to the ambient and also inversely proportional to the sum of the external thermal resistances including module substrates. While, the optimum TE element (leg) length d_{opt} is found as Eq. (2),

$$w_{\max} = \frac{Z}{4(1+m)^2}\frac{1}{A\sum\Psi}(T_s - T_a)^2 \qquad (1)$$

$$d_{opt} = m\kappa FA\sum\Psi \qquad (2)$$

$$m_{opt} = \sqrt{1+Z\overline{T}} \qquad (3)$$

 ISBN:978-2-35500-022-5

where $\Sigma\Psi$ is the sum of external resistances, A is area of substrate, κ is the thermal conductivity of TE material, and F is fractional area ratio of the TE leg (fill factor). These relations are derived for symmetric thermal contacts with hot and cold reservoirs. There are slight changes for asymmetric systems [45]. Based on this analysis, one can see that the fill factor does not affect power output until reaching less than 1% if the leg length is scaled accordingly for thermal impedance matching. This constant thermal resistance ideally yields an immediate volume reduction of the TE element itself. Without considering the parasitic losses, such as heat leakage and contact resistances, the cost per power output of TE could be reduced by 1/10,000 for 1% of fill factor. Realistic modules and power generation systems, however, still need the substrates and heat sinks with constant volume. As well as, the thermal spreading resistance increasing with reduced fill factor. Considering these impacts, the cost of the system is found for different fill factors as shown in Fig. 3. It can be seen that the reduction of thermal conductivity has the greatest impact on the $/W metric for waste recovery systems [46].

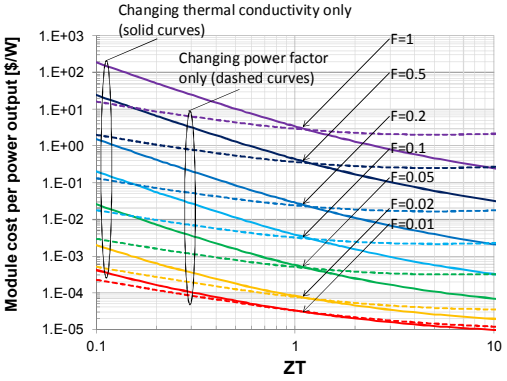

Fig. 3. Module cost performance [$/W] at the maximum power design. Thermal conductivity κ is 1.5 W/mK and power factor is 3.35×10^{-3} W/mK^2 for ZT=1. The number of elements per unit area N is 100 cm^{-2}.

IV. Hybrid Solid-State Micro-Refrigeration / Liquid Cooling

Conventional cooling by microchannel reaches the limit in the reduction of the thermal resistance due to the insensitive heat transfer coefficient to the coolant flow rate, resulting in a massively large amount of power required for a small improvement in cooling. We studied the hybrid scheme using a thermoelectric in conjunction with microchannels as shown in Fig. 4. The fundamental performance model is independent to the kinds of thermoelectric materials, whereas this particular figure shows a Si/SiGe supperlattice cooler. The total cooling power should increase by injecting an electrical current to the thermoelectric for pumping the local heat. In turn, pumping the excess heat flux at the hot spot helps to relax the requirement of the overall heat sink performance.

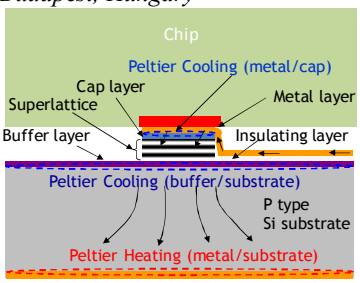

Fig. 4. Thermoelectric hybrid scheme structure diagram. vMicro-channel heat sink is not shown.

Analytic modeling allowed us to analyze the performance when we change the design of the TE element and the drive current to get the minimum cooling power to meet the junction temperature, T_j, requirement not exceeding the maximum allowable temperature, T_{j_max}. Fig. 5 shows an example of the T_j dependance on the above two design parameters.

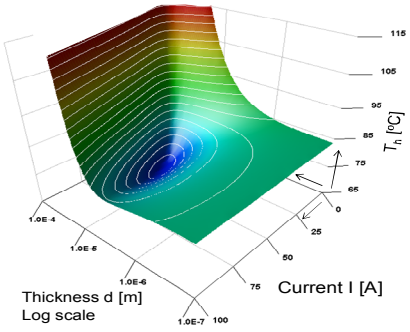

Fig. 5. The junction temperature, T_j, as a function of TE cooler thickness, d, and drive current, I. ZT=0.5 and ambient temperature T_a=35 °C are assumed.

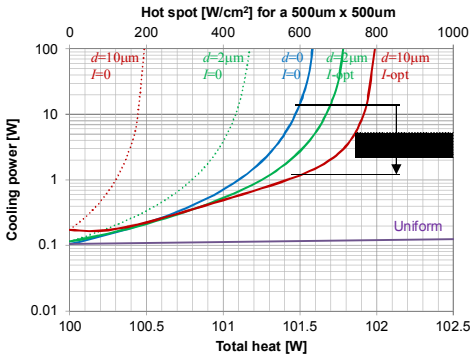

Fig. 6. Total cooling power as a function of the chip power and the hot spot heat flux. Tj_max=85 °C, ZT=0.5 are assumed.

The result shown in Fig. 6 shows that this hybrid scheme could allow us to reduce the total cooling power by nearly 1/10 of what we may need for conventional microchannel cooling at 600 W/cm^2 for a 500 μm x 500 μm single hotspot on a uniformly heated 1 cm x 1 cm chip with 100 W/cm^2.

V. Thermoreflectance Imaging Technique

Device level thermal characterization requires identifying the two-dimensional temperature gradients and the localized

 ISBN:978-2-35500-022-5

temperatures, thus, thermal mapping is important. Due to the feature size (1-10s microns) of the device with adjacent heaters at a wide range of operating temperatures, conventional Infrared (IR) imaging is not suitable. We developed a thermoreflectance imaging technique with electrical interlocking. Thermoreflectance stands for the reflectivity change versus the temperature changes of the surface. This relationship is nearly the constant. It is a material surface property for a particular wave length of the externally illuminating light [47-49]. By using an inter-lock technique, the temperature change with applied bias can be measured at the accurate timing of ON and OFF. Fig. 7 shows an example of a Si/SiGe superlattice cooler fabricated on a silicon substrate [48]. The heating load imitating the cooling target device, e.g. LSI chip with a hotspot, was fabricated on top of the TE device, so that we can identify the junction temperature.

The power demands of either energy systems or cooling are typically intermittent. The transient response characteristics cause different overall efficiencies. Therefore, transient temperature imaging is critical to determine the performance of the energy conversion devices. The electrical signal interlocking and the image interleave in software enable us to compose the frame-by-frame animation as the time line image in addition to the time response data set. Fig. 8 shows an example of time line images demonstrating the capability of sub-nano second time resolution [50].

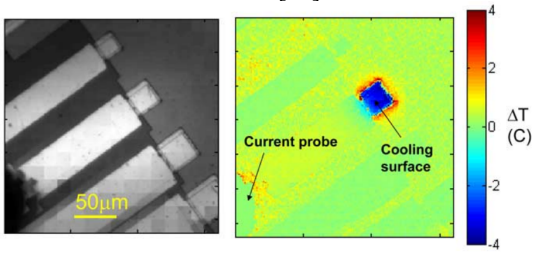

Fig. 7. Thermal image of a 50 x 50 µm^2 microrefrigerator at an applied current of 500 mA. Stage temperature is 30 °C and the device is cycled at a frequency of ~1 kHz [48].

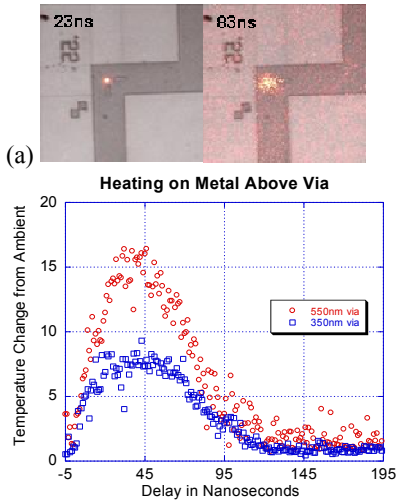

Fig. 8. Picosecond thermal imaging of sub-micron vias [50]. (a) shows the overlay of thermal image on optical image. (b) shows the temperature response to a pulsed power input.

VI. Thermal Identification of Thin Films With Time-Domain Thermoreflectance

The measurement principle of time-domain thermoreflectance is schematically illustrated in Fig. 9. Optical pulses from a femtosecond Ti:Sapphire laser (typical parameters: ~300 fs pulses, repetition rate 76-80 MHz, wavelength ~780 nm) are split into two beams undergoing separate treatment which are then recombined onto the sample under study. The 'pump' beam induces localized heating of the sample while the 'probe' beam monitors the thermally induced changes in surface reflectivity. The delay between pump and probe can be accurately varied by means of a mechanical delay line. Fitting the observed temperature decay as a function of pump-probe delay to a diffusive heat spreading model enables us to identify the unknown thermal parameters.

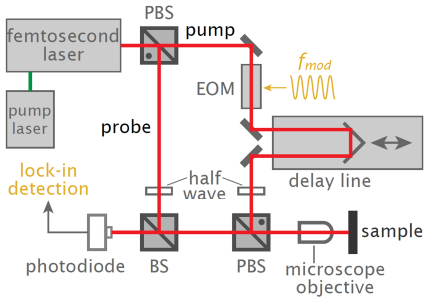

Fig. 9. Schematic principle of a typical TDTR setup for thermal characterization. EOM = electro-optic modulator, (P)BS = (polarizing) beam splitter.

A thin metallic film, typically aluminum, is deposited on top of the sample to act as transducer for the measurement (Fig. 10). The film efficiently converts the absorbed pump pulse into heat and provides a good temperature dependence of surface reflectivity under IR illumination. To achieve sufficient signal-to-noise ratios, the pump beam is modulated at a frequency f_{mod} (typically in the 1-20 MHz range) such that lock-in detection of the probe signal at the same frequency can be utilized. We note here that higher modulation frequencies correspond to shorter effective thermal penetration lengths into the sample. This is very useful for characterization of thin films as it enables one to minimize the influence of the substrate parameters on the measured thermal response. Knowledge of both in-phase, V_{in}, and out-of-phase, V_{out}, signal components on the lock-in can be exploited by using the ratio function, V_{in}/V_{out}, for further processing and analysis. This reduces experimental artifacts associated to the variation of the pump beam size with pump-probe delay and acts as a normalization process [8]. Fig. 11 gives an example of measurement data obtained for a GaAs substrate covered by a 90 nm thick aluminum film.

The thermal parameters of the sample under study can be determined by comparing the experimental data to a three dimensional heat spreading model [51]. Usually only two free parameters remain in the fitting procedure, namely the Kapitza resistance, r_K, of the aluminum/film interface and

 ISBN:978-2-35500-022-5

thermal conductivity, k, of the film. The thermal parameters of the transducer and substrate are fixed to their literature value while the transducer thickness can be determined from picosecond acoustics (see the acoustic echo in the inset of Fig. 11(a)). It is important to point out that analysis of the theoretical signal is, unfortunately, not straightforward. The single pulse response calculated by the model, i.e. the temperature response of the sample surface to a single laser pulse, must first be processed to account for the cumulative temperature effects of the multiple laser pulses and the amplitude modulation of the pump beams before comparison with experiments can be made. Derivations of the final signal form in either time or frequency domain are available elsewhere [51-53].

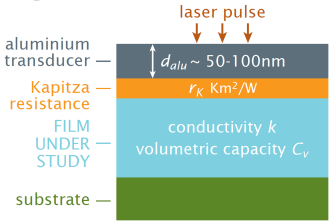

Fig. 10. Typical sample layout for TDTR thermal characterization.

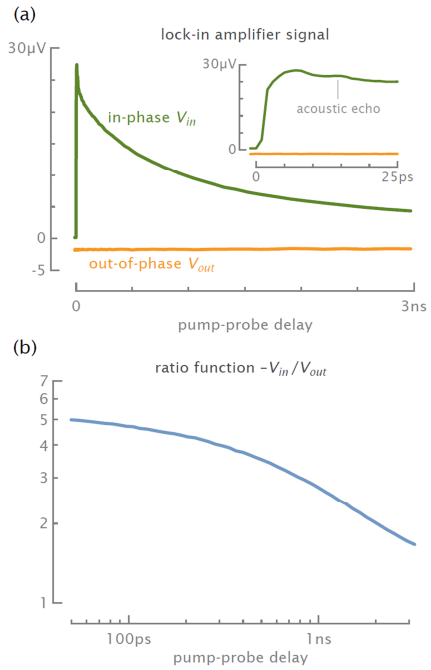

Fig. 11. Measured lock-in signals on a GaAs substrate: (a) in-phase and out-of-phase signal components with inset showing acoustic echo; (b) corresponding ratio function in double logarithmic scale.

Detailed sensitivity analyses show it is preferable to determine the Kapitza resistance from measurements over the entire available pump-probe delay at high modulation frequency. This value can then be used in the fitting procedure to determine the thermal film conductivity at other modulation frequencies. Fig. 12 illustrates identified thermal conductivities for a GaAs substrate. As we can see, an accurate estimation of the transducer thickness is crucial to obtain reliable thermal conductivity data. The picosecond acoustics provide an estimated uncertainty of ±5% on the thickness, which corresponds to a variation of roughly ±10% in the identified thermal conductivity. Errors for the laser spot size of the pump and probe beams on the sample (typically ±7%) also introduce uncertainties in the thermal conductivity, but to a much lesser extent.

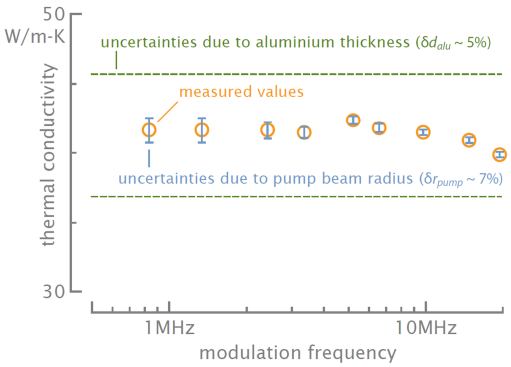

Fig. 12. Identified thermal conductivity and uncertainty contributions for GaAs substrate at different modulation frequencies.

VII. Nonthermal and Thermal Regimes of Energy Transport in Metals

Energy deposits into and propagates through a material in different ways depending on: the excitation, the structure of the material, and the nature of the energy carriers. At short time and length scales, Fourier's law becomes invalid and many non-Fourier heat conduction models, both local and nonlocal, have been developed to overcome problems associated with Fourier's model (e.g., infinite speed of propagation of heat) [54-56]. At very short time and length scales, the distinction between diffusive and ballistic regimes of energy transport becomes very relevant [57-59]. In addition to this distinction, the nonlocal effects may also become very crucial at very short length scales [56].

Using the recently developed formalism of Shastry [13], we have analyzed the transition between the nonthermal (ballistic) and thermal (ballistic-diffusive) electron energy transport in metals assuming a 1D problem in which the top free surface of the metal is excited by a delta power source [60,61]. The starting point of the analysis is the response function, N_2, introduced by Shastry [13]. This function gives a measure of the change in the energy density and hence the temperature at various points in the metal in response to the applied excitation at the top free surface of the metal and, as such, represents the energy (heat) Green's function of the metal. The Shastry-Green function, N_2, is a very simple expression in the case of a metal:

$$N_2(\omega,q)=\frac{-i+\tau_q\omega}{\omega+i\tau_q\omega^2-iD_eq^2} \qquad (4)$$

This expression is obtained by turning off the coupling factor, ξ, between the charge and energy modes. As a matter of fact, and as shown by Shastry, ξ can be expressed using the high frequency limit of the thermoelectric figure-of-merit Z^*T ($\xi=Z^*T/(1+Z^*T)$)[13], and since metals are very poor

 ISBN:978-2-35500-022-5

thermoelectric materials with a very low ZT, the decoupled limit is therefore justified. In Eq. (4), ω is the angular frequency, q is the electron wave vector, D_e is the electronic thermal diffusivity, and τ_q is the total electron scattering time, which, in general, is a function of q. The detail of the calculations can be found in references [60,61]. Here we shall focus on giving and summarizing the key results of the abovementioned analysis.

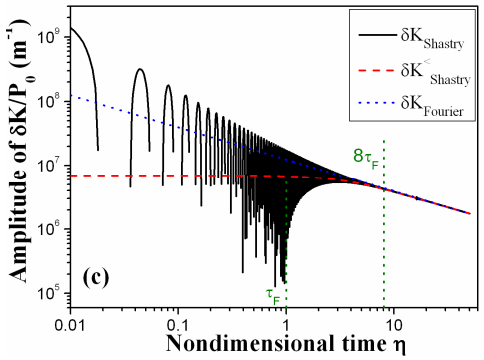

Fig. 13. Comparison between the behaviors of the thermal contributions (dashed line), the sum of the nonthermal and thermal contributions (solid line) to the total electron energy density Green's function at the top free surface of gold at room temperature, with Fourier's model (dotted line) as a function of the non-dimensional time, $\eta=t/\tau_F$.

In our treatment, we assume the case of a constant scattering time $\tau_q = \tau_F$, which we consider to be the average scattering time of electrons over the Fermi surface of the metal. We show that the total energy density Green's function $\delta K(t,x)$, which is proportional to the inverse Fourier transform of $N_2(\omega, q)$, can be expressed as a sum of two contributions; a *"nonthermal"* and *"thermal"* [60,61]. As can be seen in Fig. 13, at the top free surface of the metal, the thermal contribution $\delta K^C(\eta,0)$, undergoes two different temporal regimes. For $\eta<1$, before any scattering event happens, $\delta K^C(\eta,0)$ is almost constant, then starts decaying exponentially with time up to about $\eta\sim 8$, from which it changes the trend and starts following a Fourier type energy diffusion law. On the other hand, the nonthermal contribution $\delta K^>(\eta,0)$ (not shown in Fig. 13, instead we show the sum of the nonthermal and thermal contributions) shows a dampening oscillating behavior as a function of time. While it dominates at very short times, $\delta K^>(\eta,0)$ becomes insignificant after about $\eta\sim 8\text{-}10$. $\delta K^>(\eta,0)$ features two types of oscillations; a fast and a slow one. The fast oscillation is characterized by a period given by $\theta_F^{\text{time}}=2\sqrt{3}a/v_F$, where a refers to the metal lattice constant and v_F is the Fermi velocity. This fast oscillating behavior in the energy transport ($\theta_F^{\text{time}} \approx 1fs$ at room temperature for a typical noble metal) is a consequence of the band cut-off due to the discrete character of the crystalline lattice. This leads to Bragg reflection of electrons in a metal. This fast oscillating behavior can be viewed as an energetic analogous to the conventional Bloch oscillation in the charge density of the conduction band electrons [62,63]. On the other hand, the slow oscillation behavior has a period given by $\theta_F^{\text{time}}=4\pi\tau_F$ and it describes the nature of the thermalization process, which means the transition from the nonthermal regime to the thermal regime of energy transport. This transition occurs in a damped oscillatory manner with a pseudo-period proportional to the total scattering time of electrons.

The analysis made at the top free surface of the metal can easily be extended to any location, y. We report the spatial behaviors of the total energy density Green's function $\delta K(\eta,y)$ as calculated based on Shastry's formalism, in comparison with the Cattaneo and Fourier models [60,61]. The amplitude of $\delta K(\eta,y)$ decreases as the observation point is moved through the metal far from the excitation location (top free surface). Moreover, because of the causality requirement, the energy density vanishes for locations $y>\eta$. The locations beyond the energy pulse front remain unaltered while at locations before the front, the energy density tends to a Fourier-type behavior at long time scales.

Similarly to the temporal behavior, the spatial behavior of $\delta K(\eta,y)$ features fast and slow oscillations. The fast spatial period is given by by $\theta_F^{\text{space}}=2a$ and it is nothing other than the size of the Wigner–Seitz unit cell, which is the reciprocal of the FBZ, while the slow spatial period is proportional to the MFP ($\Gamma_F=v_F\tau_F$) of the electron, $\theta_F^{\text{space}}=(4\pi/\sqrt{3})\Gamma_F$. Similar to the oscillations in the time domain, the oscillations in the space domain describe the same sequence of physical phenomena. Namely, the nonthermal (ballistic) transport of the energy density at short time scales, when the distribution of the electronic system in the conduction band of the metal is still in a nonequilibrium state, followed by an oscillating transition to the thermal (ballistic-diffusive) regime, when the electronic distribution tends toward an equilibrium thermal distribution and a temperature can be defined. The ratio of the spatial to the temporal periods of the fast and slow oscillations is the same for both oscillation types and it is given by the speed of the energy pulse, $U=\sqrt{D_e/\tau_F}$.

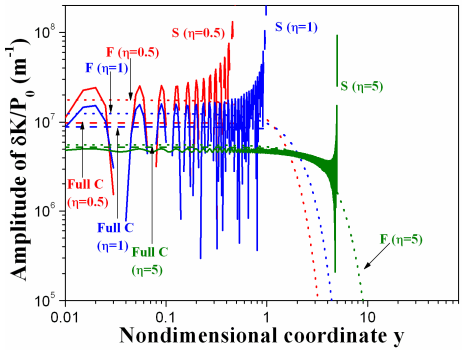

Fig. 14. Spatial behavior of the total electron energy density Green's function of gold at room temperature at different times, η, as calculated based on Shastry's model (S, solid), in comparison with Cattaneo's model (C, dashed) and Fourier's model (F, dotted). The non-dimensional coordinate in the x-axis is defined as $y=x/\sqrt{D_e\tau_F}$.

It may appear shocking or anomalous to have negative values of the electron energy density at short time scales. One should not forget, however, that at these short time scales, the electronic distribution in the conduction band of the metal is still in a non-equilibrium state and the energy density is mostly transported ballistically before it thermalizes. As the electronic distribution tends to an equilibrium thermal one,

 ISBN:978-2-35500-022-5

there is an exchange in energy density between different locations of the metal both ballistically and through diffusion (represented by D_e). This nonthermal (ballistic) transport of the energy density dampens out with time very quickly as the nonthermal regime transitions to a full diffusive thermal regime. Electron-electron interactions, not considered here, can redistribute the electrons in the momentum space, and affect the ballistic distance traveled by electrons with different wavelengths.

VIII. SUMMARY

Nanoscale electrothermal energy conversion devices have a wide range of applications. Thermoelectric devices are a viable candidate for cost-effective sustainable energy applications. Although the low energy conversion efficiency of the current TE devices limits its applications, recent advances in thermoelectric material research based on nanostructured materials have shown promising enhancement of the efficiency. The cost analysis of TE devices shows that TE devices can be as competitive as conventional mechanical energy conversion systems even with current efficiency values when it comes to cost per watt performance. A hybrid cooling scheme, combining TE micro-coolers with micro-channel liquid cooling, is very effective for removing hot spots that plague today's micro-chips. Thermal transport in thin film nanostructured materials can be precisely studied using the time-domain thermoreflectance technique. The thermoreflectance imaging technique is also useful for fast temperature mapping of sample surfaces without a scan providing sub-microsecond temporal and submicron spatial resolutions. Finally, we have applied Shastry's model to electron energy transport in metals, and interesting separation of ballistic and diffusive transports in temporal and spatial analysis is revealed due to the unique oscillatory behavior of the ballistic component in very short time and length scales.

ACKNOWLEDGMENT

A.S. acknowledges the funding from the Center for Energy Efficient Materials, an Energy Frontier Research Center funded by the U.S. Department of Energy, Office of Basic Energy Sciences under Award Number DE-SC0001009 which supported the work of B.V. and J.-H.B; DARPA/Army Research Office, Contract No. W911NF0810347 supporting the work of G.P.; and the Interconnect Focus Center, one of the five research centers funded under the Focus Center Research Program, a DARPA and Semiconductor Research Corporation Program which supported the work of Y.E. and K.Y.

REFERENCES

[1] L. E. Bell, Science 321, 1457 (2008).
[2] L. D. Hicks, M. S. Dresselhaus, Phs. Rev. B 47, 12727 (1993).
[3] C.J. Vineis, A. Shakouri, A. Majumdar, M.G. Kanatzidis, Advanced Materials 22, 3970 (2010).
[4] A. Shakouri, Annual Review of Materials Research 41, 399 (2011).
[5] K. Yazawa, A. Shakouri, Environ. Sci. Technol 45, 7548 (2011).
[6] A. Bar-Cohen, M. Arik, M. Ohadi, Proc. IEEE 94, 1549 (2006).
[7] V. Sahu, Y. Joshi, A. Federov, Proceedings of ITherm (2008).
[8] R. M. Costescu, M. A. Wall, D. G. Cahill, Phys. Rev. B 67, 054302 (2003).
[9] S. Huxtable, D. G. Cahill, V. Fauconnier, J. O. White, J.-C. Zhao, Nature Mater. 3, 298 (2004).
[10] G. Pernot, et al. Nature Mater. 9, 491 (2010).
[11] L. E. Cassels, et al., J. Vac. Sci. Technol. B 29, 03C114 (2011).
[12] P. G. Burke et al., J. Electron. Mater. 41, 948 (2012).
[13] B. S. Shastry, Rep. Prog. Phys., 72, 016501 (2009).
[14] A. Shakouri, M. Zeberjadi, Chapt. 9, in Thermal Nanosystems and Nanomaterials, ed. by S. Volz, (Springer Berlin / Heidelberg, 2009).
[15] R. Kim, S. Datta, M. S. Lundstrom, J. Appl. Phys. 105, 034506 (2009).
[16] A. Shakouri, J. E. Bowers, Appl. Phys. Lett. 71, 1234 (1997).
[17] G. D. Mahan, L. M. Woods, Phys. Rev. Lett. 80, 4016 (1998).
[18] D. Vashaee, A. Shakouri, Phys. Rev. Lett. 92, 106103 (2004).
[19] R. Kim, C. Jeong, M. S. Lundstrom, J. Appl. Phys. 107, 054502 (2010).
[20] Z. Bian et al., Phys. Rev. B 76 , 205311 (2007).
[21] J.-H. Bahk, R. B. Sadeghian, Z. Bian, A. Shakouri, J. Electron. Mater. 41, 1498 (2012).
[22] S. V. Faleev, F. Leonard, Phys. Rev. B 77, 214304 (2008).
[23] M. Zebarjadi et al., Appl. Phys. Lett. 94, 202105 (2009).
[24] J.-H. Bahk, Z. Bian, M. Zebarjadi, P. Santhanam, R. Ram, A. Shakouri, Appl. Phys. Lett. 99, 072118 (2011).
[25] J.-H. Bahk, P. Santhanam, Z. Bian, R. Ram, A. Shakouri, Appl. Phys. Lett. 100, 012102 (2012).
[26] M. Zebarjadi et al., Nano Lett. 11, 2225 (2011).
[27] J. P. Heremans et al., Science 321, 554 (2008).
[28] J. M. O. Zide et al., J. Appl. Phys. 108, 123702 (2010).
[29] R. Venkatasubramanian, E. Siivola, T. Colpitts, B. O'Quinn, Nature 413, 597 (2001).
[30] T. C. Harman, P. J. Taylor, M. P. Walsh, B. E. LaForge, Science 297, 2229 (2002).
[31] Y. K. Koh, C. J. Vineis, S. D. Calawa, M. P. Walsh, D. G. Cahill, Appl. Phys. Lett. 94 , 153101 (2009).
[32] B. Poudel et al., Science 320 , 634 (2008).
[33] A. I. Hochbaum et al., Nature 451 , 163 (2008).
[34] K. F. Hsu et al., Science 303, 818 (2004).
[35] P. F. P. Poudeu, J. D'Angelo, A. D. Downey, J. L. Short, T. P. Hogan, M. G. Kanatzidis, Angew. Chem. Int. Ed. 45 , 3835 (2006).
[36] J. Androulakis et al., J. Am. Chem. Soc. 129, 9780 (2007).
[37] Y. Pei, J. Lensch-Falk, E. S. Toberer, D. L. Medlin, G. J. Snyder, Adv. Funct. Mater. 21, 241 (2011).
[38] G. S. Nolas, J. Poon, M. Kanatzidis, Mater. Res. Soc. Bull. Vol. 31, p. 199, Mar. 2006.
[39] B. C. Sales, D. Mandrus, R.K. Williams, Science 272, 1325 (1996).
[40] A. Saramat et al., J. Appl. Phys. 99, 023708 (2006).
[41] M. S. Dresselhaus et al., Adv. Mater. 19, 1043 (2007).
[42] W. Wang et al., Appl. Phys. Lett. 93 , 193121 (2008).
[43] J.-S. Rhyee et al., Nature 459, 965 (2009).
[44] S. R. Brown, S. M. Kauzlarich, F. Gascoin, G. J. Snyder, Chem. Mater. 18, 1873 (2006).
[45] K. Yazawa and A. Shakouri, J. Appl. Phys. 111, 024509 (2012)
[46] K. Yazawa and A. Shakouri, J. Mater. Res. 27, 1211 (2012).
[47] J. Christofferson and A. Shakouri, Rev. Sci. Instrum. 76, 024903-1-6 (2005).
[48] A. Shakouri, Proc. IEEE 94 (8), 1613 (2006).
[49] K. Yazawa and A. Shakouri, Electronics Cooling Magazine Spring Issue 2011, ITEM Publications, pp. 10 (2011).
[50] J. Christofferson, K. Yazawa, A. Shakouri, Proc. 14th International Heat Transfer Conference (IHTC14) (2010).
[51] D. G. Cahill, Rev. Sci. Instrum. 75, 5119 (2004).
[52] A. J. Schmidt, X. Chen, G. Chen, Rev. Sci. Instrum. 79, 114902 (2008).
[53] S. Dilhaire, G. Pernot, G. Calbris, J.-M. Rampnoux, S. Grauby, J. Appl. Phys. 110, 114314 (2011).
[54] A. A. Joshi, A. Majumdar, J. Appl. Phys. 74, 31 (1993).
[55] F. X. Alvarez, D. Jou, Appl. Phys. Lett. 90, 083109 (2007).
[56] D. Y. Tzou, ASME J. Heat Transfer 117, 8 (1995).
[57] G. Chen, Phys. Rev. Lett. 86, 2297 (2001).
[58] G. Chen, ASME J. Heat Transfer 124, 320 (2002).
[59] M. E. Siemens, Q. Li, R. Yang, K. A. Nelson, E. H. Anderson, M. M. Murnane, H. C. Kapteyn, Nature Mater. 9, 26 (2010).
[60] Y. Ezzahri, A. Shakouri, Phys. Rev. B 79, 184303 (2009).
[61] Y. Ezzahri, A. Shakouri, ASME J. Heat Transfer 133, 072401 (2011).
[62] C. Waschke, H. G. Roskos, R. Schwedler, K. Leo, H. Kurz, K. Köhler, Phys. Rev. Lett. 70, 3319 (1993).
[63] T. Dekorsy, R. Ott, H. Kurz, K. Köhler, Phys. Rev. B 51, 17275 (1995).